Analyst

ROYAL SOCIETY OF CHEMISTRY

PAPER

View Article Online
View Journal | View Issue

Cite this: *Analyst*, 2022, **147**, 3854

Time resolved growth of (N)-polycyclic aromatic hydrocarbons in engine deposits uncovered with OrbiSIMS depth profiling†

Max K. Edney, [a] Wenshi He, [b] Emily F. Smith,[c] Edward Wilmot,[d] Jacqueline Reid,[d] Jim Barker,[d] Rian L. Griffiths, [b] Morgan R. Alexander, [b] Colin E. Snape[a] and David J. Scurr *[b]

Carbonaceous deposits are ubiquitous, being formed on surfaces in engines, fuel systems and on catalysts operating at high temperatures for hydrocarbon transformations. In internal combustion engines, their formation negatively affects worldwide vehicle emissions and fuel economy, leading to premature deaths and environmental damage. Deposit composition and formation pathways are poorly understood due to their insolubility and the intrinsic complexity of their layered carbonaceous matrix. Here, we apply the *in situ* high mass resolving power capabilities of 3D Orbitrap secondary ion mass spectrometry (3D OrbiSIMS) argon cluster depth profiling on 16 lab grown deposits and evidence common molecular distributions in deposit depth and in positions relative to the combustion chamber. We observe the products of the growth of both planar and curved polycyclic aromatic hydrocarbons to form small fullerenes over time in the engine and propose possible formation pathways which explain the molecular distributions observed. These include alkyl scission, cyclisation of aliphatic side chains and hydrogen abstraction C_2H_2 addition to form larger aromatic structures. We apply this pathway to previously unidentified nitrogen containing structures in deposits including quinolines and carbazoles. For the first time, 3D OrbiSIMS results were compared and validated with data from atmospheric pressure matrix assisted laser desorption ionization MS. The comprehensive characterization provided will help the development of a new generation of chemical additives to reduce deposits, and thus improve vehicle emissions and global air quality.

Received 11th May 2022,
Accepted 8th July 2022

DOI: 10.1039/d2an00798c

rsc.li/analyst

1. Introduction

Gasoline direct injection equipment is implemented in most light passenger vehicles today.[1,2] It is proposed that vehicles with internal combustion engines will be the most common type of passenger vehicle used in 2040. Ensuring high efficiency and low emissions of these engines for their lifetime is therefore vital. However, the breakdown and reactivity of complex fuel mixtures leads to deposit formation and their complexity partially results from the fact that they contain species derived directly from fuel and from the reactivity of these species. Deposits can lead to a catastrophic increase in emissions of gaseous pollutants, particulates and a reduced efficiency from internal combustion engines and so threaten the strive for cleaner operating vehicles.[2,3–7] Therefore, mitigating deposits will reduce the cost of fueling vehicles, reduce pollution and improve air quality. Current work aims to mitigate deposits by developing deposit solubilizing fuel additives or by suppressing adverse reactions which cause deposit formation and growth. Both strategies rely on understanding the composition, origin and formation pathways of deposits.[8–11] However, the complexity of the organic matrix and its layered nature means that probing its formation is difficult and there is limited understanding into how a thin film layer transforms into a carbonaceous deposit. Due chiefly to analytical limitations since most techniques offer only generic chemical information and cannot probe material provenance.[11] Work has been carried out into understanding how fuel mixtures undergo the initial stages of deposit formation by leakage in the injector, oxidation and adhesion to the engine component wall, leading to some initiation mechanisms being proposed.[12–14] This, however, has not been aligned with

[a]*Department of Chemical and Environmental Engineering, Faculty of Engineering, University of Nottingham, University Park, Nottingham, NG7 7RD, UK*
[b]*School of Pharmacy, University of Nottingham, University Park, Nottingham, NG7 2RD, UK. E-mail: david.scurr@nottingham.ac.uk*
[c]*Department of Chemistry, University of Nottingham, University Park, Nottingham, NG7 2RD, UK*
[d]*Innospec Ltd., Oil Sites Road, Ellesmere Port, Cheshire, CH65 4EY, UK*
†Electronic supplementary information (ESI) available. See DOI: https://doi.org/10.1039/d2an00798c

analytical data from real-world samples and has yet to explain how the reactions precipitate into a layered carbonaceous deposit. To do this we should turn to high resolution mass spectrometry (MS) techniques, such as atmospheric pressure matrix-assisted laser desorption/ionization MS (AP-MALDI-MS). This technique has been used to analyze insoluble carbonaceous materials and has revealed possible pathways of formation of polycyclic aromatic hydrocarbons (PAHs) by looking at neutral losses of ions in 1 dimensional spectra.[15,16] But this does not give spatial information with either depth nor lateral position on a given sample type. Ordered carbonaceous material has been identified in deposits using Raman spectroscopy and transmission electron microscopy,[17] which opens the possibility of formation of flat graphitic type PAHs.[18] Flat and curved PAHs can form from smaller PAHs and can go onward to form soot particles and their mechanisms of formation have been well studied.[19–21]

To advance this work we propose the use of the 3D OrbiSIMS depth profiling function to analyse deposits *in situ* on fuel injector component surfaces to establish the fate of molecules once deposited on a surface. This technique combines a low energy gas cluster ion beam to generate relatively large diagnostic secondary ions *in situ* for accurate identification and confirmation using the high mass resolving power (>240, 000) and MS/MS (fragmentation/structural characterization) capability of the Orbitrap™.[22] Not only can this approach tackle insoluble samples but it can yield *in situ* depth information, and has been successfully used by our group to elucidate the origin of key species such as alkylbenzyl sulfonates, succinimides and PAHs in such samples.[23] We will focus on probing the full chemical nature of the deposits as a function of depth which is correlated with time (*i.e.* age) of the deposit, as older deposit regions are accessed with longer sputtering times. We compare data from 16 different engine components with different origins and elucidate common molecular profiles which were comparable regardless of sample provenance. The universal nature of our data has important implications to mitigating deposits across the entire fleet of gasoline powered vehicles and will therefore bring global environmental benefit by reducing emissions and improving air quality.

2. Experimental

2.1. Engine testing bed

All gasoline direct injectors were retrieved from a vehicle with a 2.0 Liter turbocharged four-cylinder EcoTech LHU engine produced by General Motors after deliberately causing deposit formation using a dynometer test bed. The engine test was run for 100 h at steady state at 1500 rpm. At the end of the test the injector was removed and replaced, and the test was repeated using a different gasoline fuel and injector set. Images of the test rig are in Fig. S1.†

2.2. Fuels

All gasoline fuels were sourced from the USA from retail sources. A summary of the fuel composition from gas chromatography electron ionization mass spectrometry analysis performed on the gasoline fuel prior to the test is given in Fig. S1.† This summarizes the types of compounds present. We also quantified compositional data (wt%) of each compound class for all samples aside from injector 7 and 8 (see data repository). Injector 7 was run on E10 EEE Lube certification gasoline and injector 8 was run on US 'toptier' E10 retail gasoline. After retrieval, all fuel injectors were disassembled into their constituent parts for analysis, we analyzed deposits *in situ* on the injector tip and injector needle of each injector set (photographed in Fig. S1†), a total of 16 samples were analyzed from 8 injector sets. Deposits on two types of fuel injector components were interrogated in this work. First, the injector tip, which points into the combustion chamber and experiences high temperatures. Second, the injector needle, which is housed inside the injector casing, experiencing lower temperatures.

2.3. 3D Orbitrap secondary ion mass spectrometry

3D Orbitrap secondary ion mass spectrometry (3D OrbiSIMS) analysis was conducted using a Hybrid SIMS instrument (IONTOF, GmbH) with the technique outlined by Passarelli *et al.*[22] Secondary ions were collected using the Q Exactive HF Orbitrap mass analyzer (with a mass resolving power of 240 000 at m/z 200) that was calibrated using Bi_3^+ clusters to produce secondary ions from a silver strip prior to all sample measurements. In each case a 20 keV Ar_{3000}^+ gas cluster ion analysis beam was used, which was defocused to 20 μm with a cycle time of 200 μs, duty cycle of 4.4% using a target current between 0.2 and 0.3 nA, depending on the sample. Charge compensation was achieved with a low energy electron flood gun (21 V) and by regulation of the main chamber with argon gas (9×10^{-7} mbar) to delocalize any accumulation of charge surrounding the sample. A flow of pressurized nitrogen was fed to the Orbitrap™ at 12 bar. Sample data was collected over a mass range of m/z 75–1125 using SurfaceLab software (version 7.1.c (IONTOF GmbH)), with the application programming interface provided by Thermo Fisher for control of the Orbitrap MS portion of the instrument. Data processing was performed using SurfaceLab Version 7.1.c (IONTOF GmbH). On all samples, profiles were taken from different areas for each polarity. We chose areas as close to each other as possible without overlapping craters. Sample specific parameters such as analysis areas and times, total ion doses and raster mode for depth profiling and imaging experiments on all samples are tabulated in Table S2.†

Instrumental parameters used in single beam depth profiles which afforded the highest overall normalized secondary ion intensity of positively ionizing species were first determined after repeated depth profiles on injector tip 3. Here, depth profiles were performed in the same area, using short analysis times (<10 s) to allow comparison of sequential datasets without analyzing significantly different chemistries of

the deposit. A summary of this work can be found in Fig. S3.† Settings which afforded both the highest normalized ion intensity (to the total ion count) and speciation of molecular peaks were using the Ar_{3000}^+ primary ion beam at an incident energy of 20 keV with argon flooding of the main chamber to give a pressure of 9×10^{-7} mbar, a nitrogen flow pressure to the Orbitrap™ analyser of 12 bar and a flood gun energy of 21 eV.

Analysis on injector tip samples were performed in areas with high levels of carbonaceous deposit formation which yielded the highest level of secondary ion counts (determined in instrument set-up). Injector needles deposits on the 'ball' were analyzed on all internal samples, this part is closest to the combustion chamber (Fig. S1†). Three extra positions were analyzed on injector needle 1, 2 and 3 in positions subsequently further away from the combustion chamber. In all cases the apex of the injector component was analyzed and was accessed by rotating the sample holder to reveal a 'new' apex for positive and negative polarity analysis.

Combined chemical imaging and depth profiling experiments were carried out on injector tips 1, 2 & 3 using the same settings as single beam depth profiles. Chemical imaging, where rastering of the primary ion beam over the analysis area and taking mass spectra at different points to build up an image of ion intensity over the area was performed using an Ar_{3000}^+ analysis beam in random raster over a 300 μm^2 area with a non-interlaced border. Acquisition times and resolution are detailed in Table S2.† Secondary ion images were then cropped to 200 μm^2, normalized to the total ion image, and scaled to match the intensity at both depths.

MS/MS spectra were all acquired over an analysis time between 10 s and 50 s in an area of 300 μm^2 using sawtooth raster mode. Mass windows were between 1 u and 10 u and normalized collision energies were between 10 eV and 100 eV depending on the isolated ion of interest.

2.4. Chemical filtering

SIMS-MFP version 1.1 (molecular formula prediction) software (MATLAB 2021A) was used to assign species based on elemental compositions – this is an in-house software package described in previous work by this group.[24] The software takes an inputted data file (either a spectra output after a peak search or a depth profile dataset) and the user simply inserts the elemental constraints (type and number of each element) they wish to apply to the search. SIMS-MFP then assigns species which fit under the pre-defined deviation (2 ppm here) and plots the carbon number *versus* the double bond equivalence value of each possible assignment. Here spectra outputs were used after applying a peak search using SurfaceLab software (IONTOF, GmbH). Elemental constraints used in the search are detailed in the manuscript.

2.5. Atmospheric pressure matrix-assisted laser desorption/ionization high-resolution mass spectrometry

10 mg of the deposits were weighed after scraping it off the injector tip substrate using a scalpel. This was suspended in 1 ml of tetrahydrofuran (THF) and diluted further to create a 1 mg ml^{-1} concentration. A 0.5 μL drop was spotted onto an ABI Opti-TOF 192-well target plate and on top of this spot (once dried for 10 minutes) a 1 μL of 2,5-dihydroxybenzoic acid (DHB) or tetracyanoquinodimethane (TCNQ) (depending on the experiment) matrix was added, at a concentration of 5 mg ml^{-1} in THF. A Q Exactive Plus hybrid quadrupole-Orbitrap mass spectrometer (Thermo Scientific, San Jose, USA) was coupled to an AP-MALDI source (MassTech Inc., Columbia, MD). Target-ng software (MassTech) was used to control the XY stage motion and operation of the laser. The source utilized a diode-pumped solid-state Nd:YAG laser (λ = 355 nm) operating at a 0.1–10 kHz repetition rate. Maximum laser pulse energy was 3 μJ at a 1 kHz repetition rate. A beam attenuator was used to adjust laser energy. The voltage applied between the MALDI plate and inlet capillary of mass spectrometer was 4 kV. The distance between the plate and the capillary was 3 mm. The inlet capillary was set to 400 °C.[25] Each dried-droplet spot was scanned with a 50 μm wide laser spot. Mass spectra were acquired in a positive-ion mode with mass resolving power up to 180 000 at *m*/*z* 200 and a mass range of *m*/*z* 150–1500. Tandem MS parameters were the following: mass resolving power: 15 000; max injection time: 200 ms; AGC target was switched on: isolation width: 1 Da; HCD: 20 (normalized collision energy, NCE). Data was acquired and analyzed using Tune and Xcalibur software (Thermo Fisher Scientific, Waltham, MA). Species identification was carried out in Xcalibur 3.1 software with a 6 ppm mass accuracy threshold. In all cases 3 analytical repeats were taken on different areas of the sample spot.

2.6. X-ray photoelectron spectroscopy

In this work we analysed an area on the side wall of the carbonaceous injector tip deposit from injector 1 and 2. We present data from X-ray photoelectron spectroscopy (XPS) in conjunction with an argon gas cluster ion beam etching of both deposits. Samples were mounted on a standard Kratos sample bar (13 cm × 1.5 cm) using double-sided adhesive non-conducting tape. Samples were then subjected to XPS analysis using the Kratos AXIS ULTRA DLD liquid phase photoelectron spectrometer (LiPPS) with a monochromated Al Kα X-ray source (1486.6 eV) with a source power of 120 W. Gas cluster ion beam etching (20 keV, Ar_{500}^+ cluster beam) over etch area of 0.75 mm^2 on the injector tip deposit was performed prior to analysis for a cumulative etch time of 2787 s for Injector tip 1 and 8253 s for Injector tip 2. The XPS spectra for both samples were then acquired with photoelectrons collected using the electrostatic lens mode with a circular aperture of 110 μm. We used the optical camera to ensure the analysis area was central in the etched crater of the etched injector tip deposit. Spectra were acquired with the Kratos VISION II software. Low-resolution survey spectra of both samples were recorded between a binding energy range of 1200 to −5 eV, a charge neutralizer filament was used to prevent surface charging; the pass energy was 160 eV, both with a step energy of 1 eV. The spectra were charge corrected to the surface C 1s peak (adventitious carbon)

set to 285 eV and used to estimate the total atomic% of the detected elements using CasaXPS (version 2.3.22 PR1.0) software. Peak positions were referenced to the XPS reference pages of XPSFitting.

2.7. Miscellaneous

Chemical structures were drawn in ChemDraw 14.0.

Graphs were plotted in Veusz (Version 3.2.1, Jeremy Sanders) or were exported from SurfaceLab (version 7.1).

3. Results and discussion

3.1. Time resolved growth of flat and curved PAHs

Engine deposits were 'grown' in a controlled engine testing rig (Fig. 1a) using conventional gasolines of differing compositions (GC-MS analysis of the fuel is summarized in Fig. S1 and ESI†), which varied by the types of olefins or indene compounds they contained as well as quantified compositions of each class. Work has been done using 3D OrbiSIMS to define the optimum analytical conditions for biological samples,[22,26] however, little has been done on petroleomics type samples. As a result, we first performed 3D OrbiSIMS experiments on one of the grown deposits by varying experimental parameters inlcluding Ar cluster size and energy, pressure of nitrogen feed to the Orbitrap analysers collision cell, and Ar pressure for charge compensation. We assesed performance by looking at the ion intensity of molecular ions of known species explored in previous work.[23] A description of the optimization experiments is in ESI note 1 & Fig. S3.† Subsequently we performed 3D OrbiSIMS depth profiling on all 16 deposits using these determined settings. Positive secondary ion data from deposits on injector tip 1 is shown in Fig. 1 and was representative of data from all other injector tip samples.

3D OrbiSIMS depth profiling data was assessed using a chemical filtering approach (described in previous work by this group[24]) to comprehensively account for the composition of the gasoline deposits. We propose formation pathways of deposit buildup by profiling into older deposit zones and elucidating the reasons for differences in observed chemistries between older and newer areas of the deposit (Fig. 1b). From the total number of CH species, uncovered by chemical filtering, we accurately assigned radical cations ($[M]^{+\bullet}$) of PAHs up to masses >m/z 1000 using accurate mass which corresponded to known structures.[27] Injector tip 2, 5 and 8 had the highest mass PAHs (Fig. S6†). Of note is the assignment of molecular ions for 5-membered PAHs in all tip deposits including (in order of size) fluorene ($C_{13}H_{10}^{+}$, m/z 166.0776), cyclopentapyrene ($C_{18}H_{10}$, m/z 226.0777), benzofluoranthene ($C_{20}H_{12}$, m/z 252.0933) and corannulene ($C_{20}H_{10}$, m/z 250.0776) (Table S5†). We next confirmed the identity of several key PAHs not seen in deposits previously using MS/MS experiments, including secondary ions at m/z 202.07755 (pyrene), m/z 178.0776 (anthracene), corannulene, m/z 300.0932 (coronene) and m/z 394.0778 (ovalene) by assigning neutral losses of functional groups including C_n and C_nH (Fig. S7†). These were also observed in MS/MS experiments using other MS techniques on the same ions.[28,29] Here, MS/MS spectra of coronene and coranulene included several CHNO containing species, which was attributed to the inclusion of intense CHNO containing species in the isolation window due to low parent ion intensity requiring a wider isolation window (Fig. S7†).

3D OrbiSIMS depth profiles of the deposits on a substrate showed lower mass PAHs are more prevalent nearer the deposit surface (newly deposited region) compared with higher mass PAHs. Shown by the stark difference between depth prevalence of naphthalene ($C_{10}H_8^{+}$) and hexabenzocoronene ($C_{42}H_{18}^{+}$) in Fig. 1b. We attribute this to the formation of larger PAHs over time once fuel is deposited on the injector substrate. Depth profiles of injector tip 1 and all others showed this growth of PAHs throughout the deposit depth, despite the samples being derived from different fuels (Fig. S8†). The trend also held for 5-membered PAHs with larger structures being prevalent in the lower depth (Fig. S9†). Comparison of mass spectra at the surface and a lower depth after sputtering indicated much higher masses of CH species in lower layers (black in Fig. 1c). Using chemical filtering we also identified N containing aromatics (including *N*-PAHs) and noted an increase in their intensity after sputtering (red in Fig. 1c), their importance is discussed in the next section. It has long-been hypothesized that PAH growth occurs during deposit formation but has never been shown. The presence of alkylated benzene in high concentrations in the initial seeding fuel opens the possibility of cyclisation of alkyl chains to form larger aromatic structures (Fig. S1 and ESI†).[16,30,31] Depth profiles of species with both an aliphatic and aromatic content fits with the hypothesis too as they were only present at the deposits surface (Fig. S10 and Table S11†).

Using depth profiling trends, we can then move forward and link possible formation pathways from previous studies to explain deposit buildup. In all mass spectra we identified a repeating mass difference between PAHs corresponding to an alternating C_2 and C_2H_2. We illustrated this for the growth of coronene from accurate masses of ions in injector tip 2 in Fig. 1d and show this was present for other samples in Fig. S12.† This is consistent with a hydrogen abstraction acetylene addition (HACA) growth mechanism (Fig. 1d),[28] a widely studied mechanism in the buildup of PAHs[21] which has been proposed in the buildup of coal-tar pitch and other carbonaceous materials previously.[15,32,33] 5-Membered rings such as those found here have been shown to form from the direct involvement of acetylene in the HACA reaction from mechanistic studies.[34] The presence of indene means this is a likely precursor to 5-membered PAH formation (Fig. S1 and ESI†). Acetylene is likely sourced from the pyrolysis of hydrocarbons in the engine as has been shown.[35,36] It is important to state that we are not observing radical intermediates and many formation mechanisms are possible such as addition of phenyl and subsequent alkyl cyclization,[37] or direct addition of vinylacetylene (C_4H_2).[21]

The presence of 5-membered PAHs also opens the possibility of formation of curved PAHs or fullerenes since the

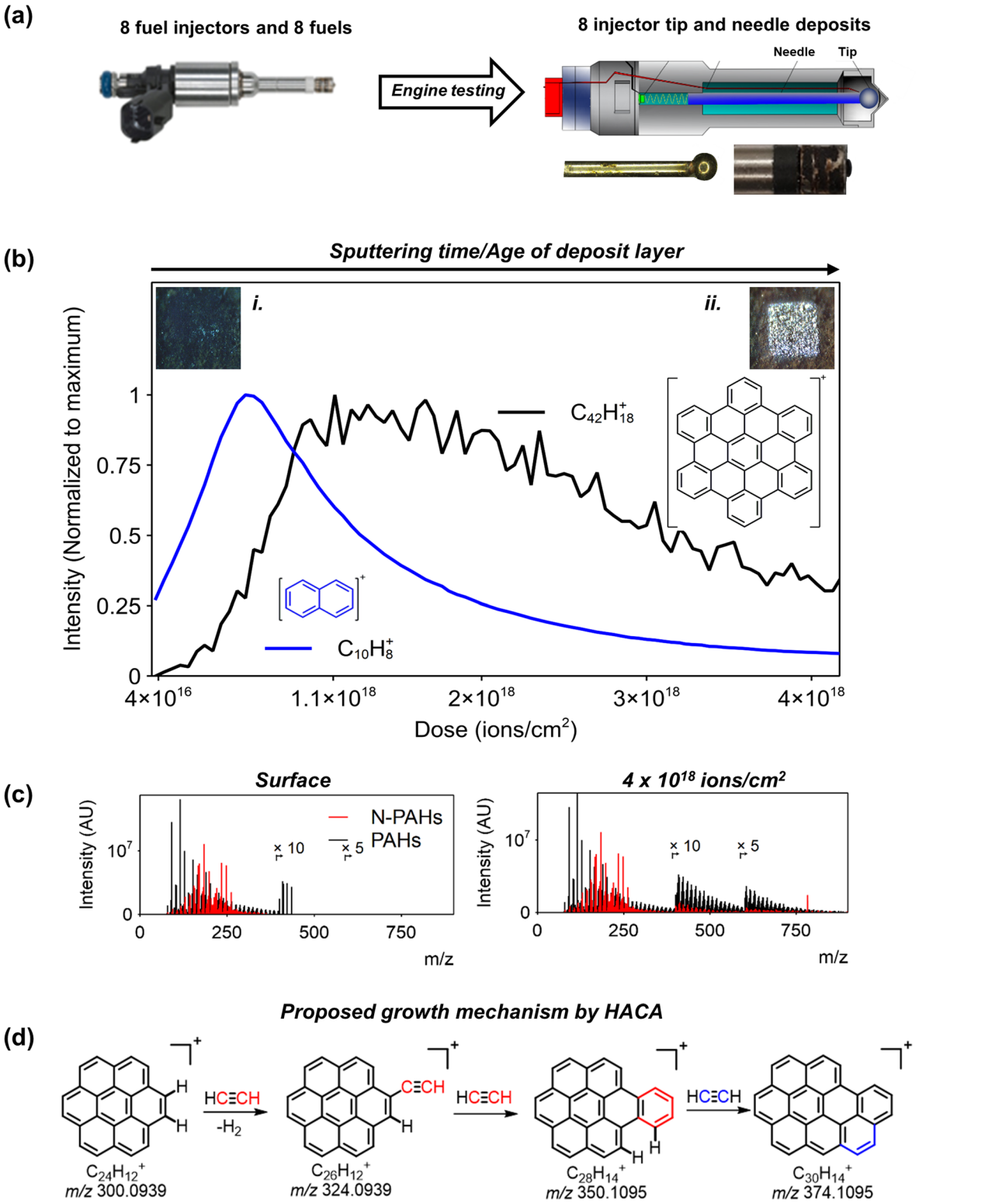

Fig. 1 (A) Schematic of the fuel injector and key components studied in this work. (b) 3D OrbiSIMS depth profiles from injector tip 2 showing the profiles of hexabenzocoronene ($C_{42}H_{18}^+$) and naphthalene ($C_{10}H_8^+$). Optical images taken from (i) before and (ii) after sputtering are displayed. (c) Depth profile accumulation spectra (normalized to maximum) from two portions of the depth profile displayed in the region of *m/z* 75–1125. Species were annotated putatively using a chemical filtering technique (molecular formula prediction), in black are ions annotated with a formula of $C_nH_n^+$ and in red we annotate those ions with a formula of $C_nH_nN^+$. (d) A proposed growth pathway of the build-up of PAHs *via* hydrogen abstraction acetylene addition (HACA), illustrated as an example from coronene using peaks identified in the 3D OrbiSIMS spectra. AU, arbitrary units.

strained 5-membered ring causes curvature in the PAH structure.[19,20] We found low intensity peaks corresponding to molecular ions for the smallest fullerenes, C_{24}^+ and C_{28}^+, in injector tip 2, 5 and 8 (Fig. S13†). Notably these samples had the highest accurately assignable maximum mass of PAHs as shown by the summary of CH species plots in Fig. S6.† Further, depth profiles from these samples showed prevalence of fullerenes in the lowest portion of the deposit, even after large PAHs such as $C_{78}H_{26}^+$ (Fig. S13†). We postulate that one destination of PAH growth in engine deposits is fullerenes and overall show the growth of carbonaceous deposits involves formation of PAHs into large flat PAHs, curved PAHs and fullerenes over time.

The ballistic effect of SIMS may mean that we are observing smaller fragments of the 'true' maximum assignable mass of key ions such as PAHs. To compare data to a more established technique with different ionization mechanisms we ran AP-MALDI analysis using a TCNQ matrix on the deposit after scraping it off the injector substrate. This is the first comparison between these techniques. Spectra from the deposit from injector tip 5 (chosen as this had the most amount of visible deposit to scrape off for analysis) showed many PAHs observed in 3D OrbiSIMS, shown by plotting the carbon number *versus* double bond equivalence value of possible CH containing ions using molecular formula prediction (Fig. S14†). In comparing this data to the AP-MALDI analysis we note several differences. Firstly, the maximum mass of accurately assignable PAH identified, $C_{90}H_{26}^+$ and $C_{114}H_{38}^+$ for 3D OrbiSIMS (within a 2 ppm error) and AP-MALDI (within a 5 ppm error) respectively, spectra and putative structures are shown in Fig. 2. Importantly, the similar maximum mass of assigned PAH in these systems validates our analytical approach using 3D OrbiSIMS for assigning PAH structures, but also in the wider context of SIMS analysis as 3D OrbiSIMS appears to be generating a comparable dataset to an established AP-MALDI approach. Secondly, we observed fewer ions *via* AP-MALDI than SIMS, which is expected as it is a softer ionization method, producing more intact ions and fewer fragments. Finally, it is observed that ionized species in AP-MALDI have a higher carbon number to double bond equivalence ratio (Fig. S14†) as compared with 3D OrbiSIMS, which are indicative of archipelago/island type PAH structures which contain alkyl chains between clusters of condensed PAHs. It is likely that SIMS is fragmenting these species to isolate only purely condensed PAHs or those with only short alkyl chains (detailed in Fig. S11†).

The 3D OrbiSIMS depth profiles acquired on samples were all relatively long (some >24 h) and therefore a possibility with exposure to a sputtering beam for this time is that some of the observed chemical changes in the profiles are resulting from this sputtering instead of representing real chemical differences. To explore this, we prized an intact piece of the deposit off the injector substrate which could be interrogated on either side with short analysis times (Fig. S15†). We then performed relatively short (30 scans) 3D OrbiSIMS analyses on the upper and underside of the extracted sample (with three analytical analyses). Application of chemical filtering (molecular formula prediction and plotting double bond equivalence *versus* carbon number) showed higher maximum masses of PAHs on the underside of the deposit. Small PAHs were present on both sides with comparable intensity, medium mass PAHs (up to $C_{42}H_{18}^+$) were present on both sides but were less intense on the upper side (Fig. S15†). PAHs above $C_{42}H_{18}^+$ were only present on the underside. Hence, we are confident that observed chemistries are genuine and not due to the Ar_{3000}^+ sputtering induced chemical changes to the sample. This is in agreement with other SIMS studies of organic materials.[38,39] Chemical imaging of injector tip 1, 2 and 3 at the surface and a lower deposit depth after sputtering showed a different lateral distribution of high and low mass PAHs, suggesting they are representative of unique species and not fragments of one another (Fig. S16†). Overall, this demonstrates that molecular differences shown in the depth profile represent true sample chemistry differences and indeed that 3D OrbiSIMS can probe the time resolved growth of insoluble materials formed on a surface.

3.2. Formation of aromatic nitrogen species in deposits

In all cases the most intensely ionizing species in 3D OrbiSIMS spectra were those containing 1 N-atom. Despite

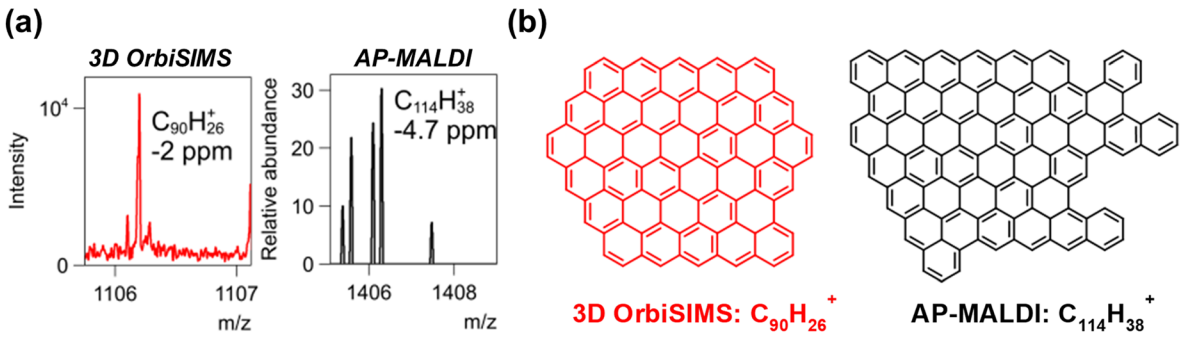

Fig. 2 Comparison of the accurately assigned maximum mass of polycyclic aromatic hydrocarbons in 3D OrbiSIMS and AP-MALDI from tip deposit 5. (a) Spectra of the maximum assigned peak with accuracy data shown. (b) Putatively assigned structures of the highest mass polycyclic aromatic hydrocarbon assigned from each technique.

crude oil containing quinolines and carbazoles naturally,[40,41] the level of N in gasoline is restricted to the ppm scale due to poor storage capabilities, adverse reactivities and effects on NOx emissions.[42,43] To accurately assess the quantified depth distribution of N we used XPS with an Ar sputtering beam on deposit 1 and 2 (Fig. S17†). In both cases the level of nitrogen increased in lower layers with a maximum contribution of 4% in injector deposit 1 (Fig. 3a), with no nitrogen at the surface of the deposit. This suggests it is introduced after initial deposition of fuel on the injector substrate, hence they are of particular interest in this work.

Intense secondary ions in 3D OrbiSIMS spectra were identified and assigned to nitrogen containing moieties which are summarized in Fig. 3b. Chemical images were used to distinguish them by their spatial distribution (ion data for other samples are in Table S18†). We first determined that these general moieties explained the significant molecular distributions in deposits using chemical filtering to annotate all species containing CHN_x (where $x = 1$), finding that deposit 5 had the most secondary ions attributable to this formula (Fig. S19†). In all samples we assigned a range of *N*-substituted PAHs (*N*-PAHs) as $[M + H]^+$ ions including benzoquinolines up to $C_{35}H_{18}N^+$ (−0.6 ppm) (Fig. 3b), suggesting addition of up to 10 benzyl units on the heterocyclic core. We performed MS/MS on key ions, results from quinoline ($C_9H_8N^+$) and benzoquinoline ($C_{13}H_{10}N^+$) confirmed the assignment with a loss of $[M - CHN]^+$, characteristic of N-aromatics (Fig. S20†).[44] Alkylated quinolines secondary ions were identified in all samples up to $C_{43}H_{76}N^+$ (−0.5 ppm). MS/MS of $C_{11}H_{12}N^+$ and $C_{10}H_{10}N^+$ both showed alkyl and CHN losses (Fig. S20†). Carbazoles were again common and identified up to $C_{28}H_{18}N^+$ (−0.8 ppm) (Fig. 3b), MS/MS of $C_{12}H_{10}N^+$ and $C_{16}H_{12}N^+$ both showed losses of pyridine $[M - CHN]^+$ and ethylene $[M - C_2H_2]^+$ as observed on reference samples.[45] The most intensely ionizing N-containing species in all samples were those with a generic proposed formula of $[C_5H_5N(C_6H_5)(C_nH_{(2n+1)})]^+$ with an alkyl chain length up to $C_{25}H_{51}$ (Fig. 3b). MS/MS of $C_{13}H_{14}N^+$ showed losses corresponding to the alkyl chain ($[M - CH_3]^+$), pyridine group, and a CH aromatic fragment. Together this data suggests an alkylated phenyl pyridine structure (Fig. 3b) which is structurally equivalent to a biphenyl unit, commonly observed in combustion of pure hydrocarbons.[30]

AP-MALDI using DHB matrix on deposit 5 (total of 3 analytical repeats) showed that for purely aromatic N-species (quinolines *etc.*) the maximum masses of assigned ions were within a few carbon numbers. For species with aliphatic components (alkyl phenyl pyridine and alkyl quinolines) there were differences between analytical repeats on different deposit areas (Fig. S21†). We repeated the experiments using TCNQ matrix and found higher maximum masses for purely aromatic groups compared to DHB. However, for species with an aliphatic component, there was a lower maximum mass (Fig. S21†). This variation of maximum mass is evidently based on the technique and highlights the importance of matrix selection for different chemical classes (as is typical of this approach). However, in each case the maximum mass of aromatic N species, which is the focus of this work, was within approximately 1–3 aromatic rings Fig. S21b.†

Next, to investigate the origin of N-species we present 3D OrbiSIMS depth profiles of compound classes from deposit tip 2 in Fig. 3b. The spatial distribution of ions captured by chemical imaging enabled us to separate ions into different classes (Fig. 3b). The formation of small *N*-PAHs species such as quinoline can occur by gas phase reaction of acetylene ($C_2H_2^{\bullet}$) and pyridyl ($C_5H_4N^{\bullet}$) radicals in high temperature conditions (700 K).[46,47] Depth profiles and a suggested scheme of these ions correlate with expected prevalence as the 'reactant' alkylated benzyl secondary ion ($C_9H_{13}^+$, **2** in Fig. 3c). These alkylated benzene compounds were present in the initial fuel composition (Fig. S1† and suplementary information). This class of ions in deposits with enough intensity for an informative depth profile (all except injector tips 3 and 4) were present at the uppermost deposit layers. Again, it is important to state we are observing numbered products in the scheme (positive ions) and proposing radical intermediates to form the observed secondary ions. An example alkylated pyridyl ion ($C_{11}H_{18}N^+$, **1** in Fig. 3c) increased in intensity during sputtering, suggesting it is formed after initial deposit initiation and is consistent with the hypothesis that the origin of N-containing species is from reaction with air after deposit formation initiation and not from the fuel. The reaction of these two can then form the alkyl phenyl pyridine species observed in SIMS data (example shown as **4** in Fig. 3c) and is analogous to the formation of biphenyl species by free radical pyrolysis of 2 benzyl units (which has been well documented[30]). The electron withdrawing nature of the nitrogen can promote reaction at the *ortho* position on the ring, hence our suggested structure in the scheme ($C_{13}H_{14}N^+$, **4** in Fig. 3c).

Separately, the initial pyridyl ion (**1** in Fig. 3c) can undergo HACA to form alkylated quinolines ($C_{10}H_{10}N^+$, **3** in Fig. 3c); both the alkyl phenyl pyridines and alkyl quinolines were more prevalent in deposit layers lower than the suggested 'reagents'. Quinoline ($C_9H_8N^+$, **5** in Fig. 3c) was prevalent after alkyl quinolines, suggesting that scission of the alkyl chains occurs next. The specific free-radical mechanism of the alkyl scission (−R in Fig. 3) is complex but generally follows subsequent reduction of carbon chain length to form a radical and an unsaturated species.[31,48,49] The formation of the positive secondary ion observed in the SIMS data likely arises from addition of a proton to the radical on the terminal carbon on the chain. Next, the formation of benzoquinoline, $C_{13}H_{10}N^+$ (**6** in Fig. 3c) can be accessed by HACA from both the quinoline and the alkyl phenyl pyridine ion and had expected depth behavior. Finally, the buildup of larger *N*-PAHs, exemplified by the ions $C_{23}H_{14}N^+$ and $C_{31}H_{16}N^+$ (**7** and **8**, respectively in Fig. 3c), suggested through HACA, is shown with higher mass aromatics to have prevalence at lower layers which is analogous to PAH growth. This trend was common for all other injector tip deposits despite different sample provenance (Fig. S22†).

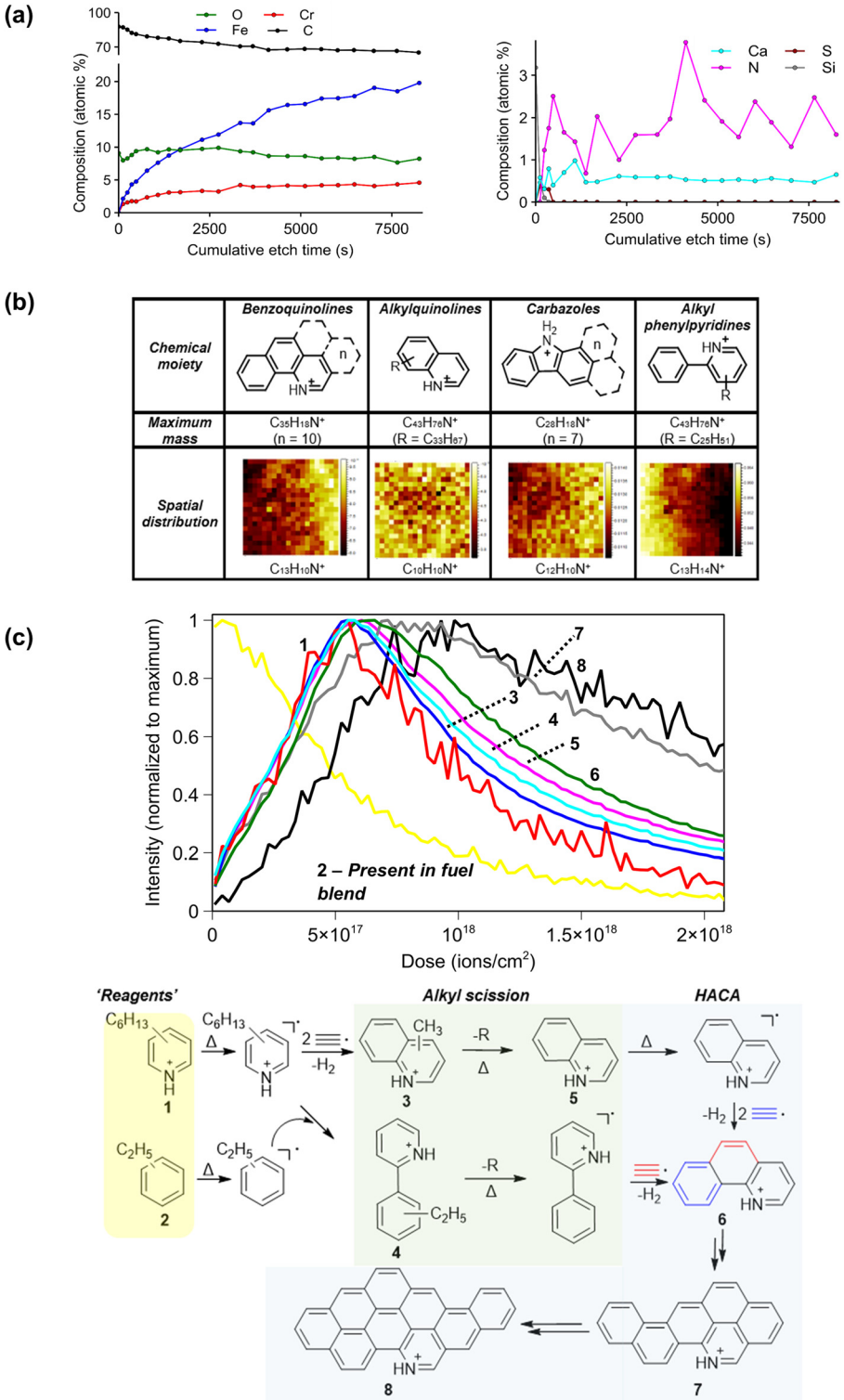

Fig. 3 Speciation of N-containing species and uncovering possible formation pathways using 3D OrbiSIMS depth profiles of key ions. (a) X-ray photoelectron spectroscopy Ar_{500}^+ depth profiling results from injector tip 2. (b) Table detailing general identified compound classes with maximum mass ions error data shown (*n* denotes the number of fused 6 membered rings on the heterocyclic core, R = saturated alkyl chain). Chemical images (200 μm^2) from the surface of the deposit from injector tip 2 of an exemplar ion belonging to each molecular series is displayed with the ion formula shown. (c) Above, 3D OrbiSIMS Ar_{3000}^+ depth profiles (normalized to maximum) of nitrogen containing species, below, a suggested formation pathway that links the species based on their prevalence in the deposit depth. Numbered products are observed and correspond to those in the depth profiles.

3.3. Analysis of thin-film deposits to probe early stages of deposit formation

Thin-film injector needle deposits were retrieved from engine testing and allow us to explore the effect of temperature across the components surface since one end of the needle is closer to the combustion chamber (marked by 'High T' and 'Low T' in Fig. 4c). It has long been thought that these are precursors to the carbonaceous deposits seen in injector tips. We applied chemical filtering to 3D OrbiSIMS depth profile accumulation spectra from the ball (orange box in Fig. 4) on all 8 needle samples, and identified many PAHs, but were accurately assigned up to a lower maximum mass than the tip deposits (Fig. S6†). This is likely due to the reduced temperature experienced by this component, showing how the key signpost in assessing deposit severity is the PAH size distribution. To further probe the temperature effect, we performed relatively short (<200 s) 3D OrbiSIMS analyses on 3 positions along the needle (at different distances to the combustion chamber) on 3 of the samples. The variation in the presence of three example PAHs of varying size are plotted in Fig. 4a.

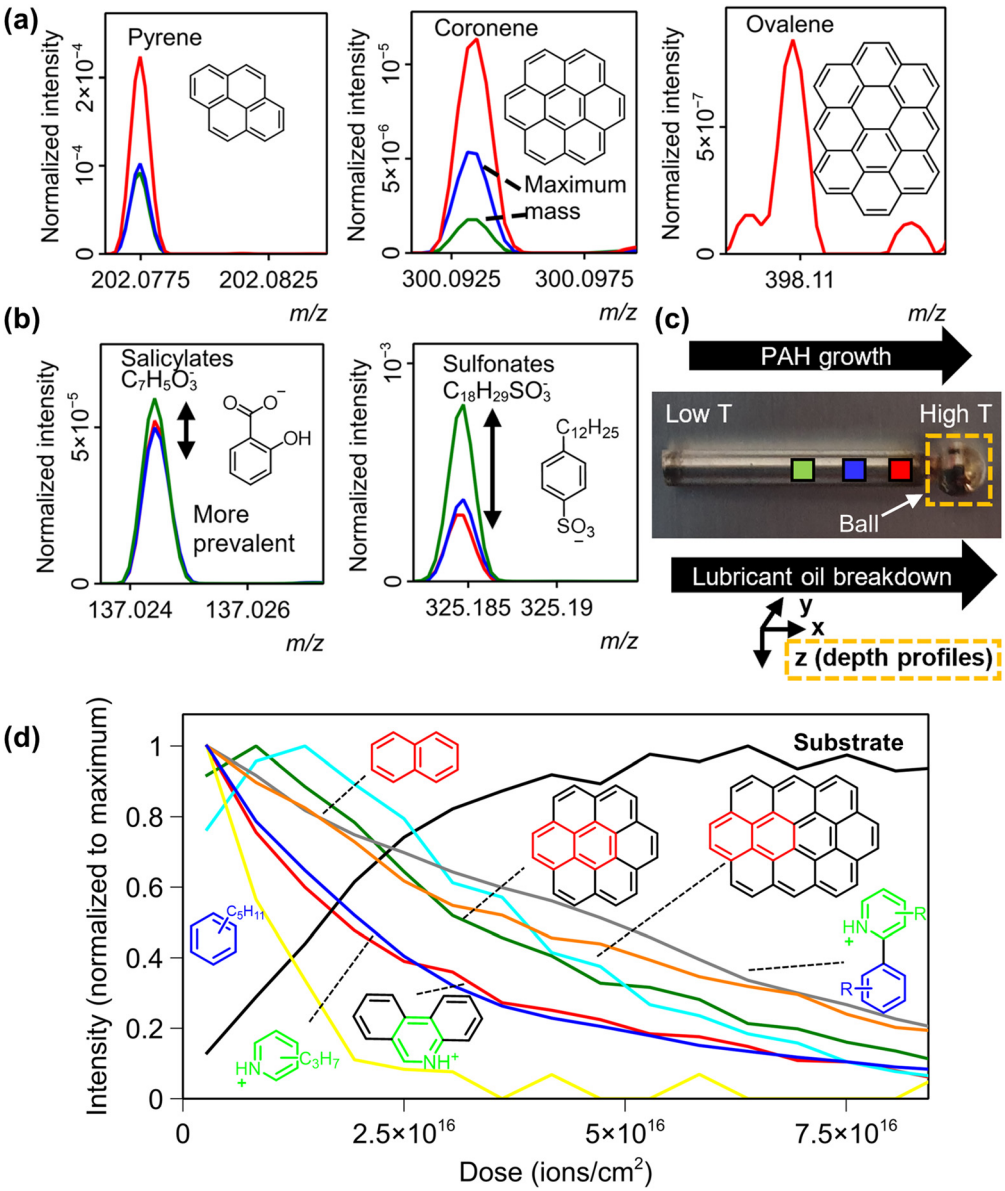

Fig. 4 Tracking molecular transformations *in situ* on a fuel injector needle. (a) 3D OrbiSIMS depth profile accumulation spectra from different positions along injector needle 3 of PAHs, pyrene ($C_{16}H_{10}^+$), coronene ($C_{24}H_{12}^+$) and ovalene ($C_{32}H_{14}^+$) (left to right) intensity and maximum mass at each position. (b) Intensities of salicylates ($C_7H_5O_3^-$) and sulfonates ($C_{18}H_{29}SO_3^-$). (c) Photograph of injector needle 3 with color-coded boxes representing each analysis area (not to scale). (d) Depth profiles from the ball of the injector needle (orange box in c).

The intensity of PAHs increased closer to the combustion chamber, as did their maximum mass, for example we observed coronene in each position, whereas ovalene was only identified in position 1 (Fig. 4a and Fig. S25b† for other samples), showing how the effect of temperature can lead to enhanced growth of PAHs across a surface. Depth profiles from the injector ball (orange box in Fig. 4c) of injector needle 3 correlate with those of the injector tip deposits (Fig. S8† for PAHs and Fig. S22† for *N*-PAHs), where larger PAHs and *N*-PAHs were more prevalent at lower depths (Fig. 4d). In all cases the maximum mass of *N*-PAHs were relatively uniform across the surface (Fig. S23†), suggesting their formation is not just tied to temperature and breakdown of fuel. It is plausible that with air being a likely origin of N in the system that access to it is another rate determining step, and in the high-fuel pressure injector needle the scarcity of air makes it the limiting step, conversely to the external deposits with access to 'excess' air.

We accurately identified lubricant oil derived alkyl benzyl sulfonates which were found in previous work,[23] and alkyl salicylates ($[C_7H_5O_3C_nH_{(2n+1)}]^-$). These were confirmed using MS/MS in these systems (Fig. S24†) by observing characteristic neutral losses of –CO, $–CO_2$ and –OH functionalities (negative ion details can be found in Table S4†). Conversely to PAH formation their intensity decreased in positions closer to the combustion chamber (Fig. 4b and Fig. S25a†). Overall, this work has shown how we can map the time resolved growth of aromatic structures and breakdown of other species with an *in situ* analysis technique and infer possible formation mechanisms. Our repeated identification of the same chemical structures for fuel deposits, regardless of the input fuel in the engine test has significant implications for worldwide efforts to understand deposit formation and mitigate them.

4. Conclusions

In this study we comprehensively characterized a range of lab-grown gasoline deposits *in situ* on engine components which were derived from different fuels using 3D OrbiSIMS accurate mass assignments, MS/MS, AP-MALDI and XPS. This enabled identification of a plethora of species previously unseen in these materials including structurally diverse PAHs and nitrogen containing species such as alkylated quinolines, carbazoles and biphenyl derivatives. We used depth profiling behaviour of key species to explain their formation over time by possible formation pathways, following a trend of initial alkyl scission and HACA which explains the growth of large aromatic structured, most notably the growth of flat and curved PAHs to small fullerenes in the engine. We also provide a first-time comparison of 3D OrbiSIMS to AP-MALDI data, demonstrating the presence of similar maximum mass species. Importantly, pathways of deposit formation are shown to be common regardless of the fuel used. Our new insights will contribute to several mitigation strategies, for example, synthesizing next-generation additives to solubilize deposits, which is particularly viable now we have a far-greater understanding of deposit matrix composition. Helping to mitigate deposits will lead to longer-term benefits such as increased internal combustion engine efficiency, reduced pollution and improved global air quality.

Author contributions

D. J. S., J. B., C. E. S. and M. K. E. planned and coordinated the work. M. K. E. conducted 3D OrbiSIMS experiments. M. K. E., W. H. and R. L. G. conducted AP-MALDI experiments. E. F. S. conducted XPS experiments. All authors aided in interpreting the analytical data. M. K. E. wrote the manuscript and all authors helped in its edits.

Data and materials availability

Data not found in the ESI† can be found in the University of Nottingham data repository (**https://doi.org/10.17639/nott.7221**).

Conflicts of interest

The authors declare no conflicts of interest which may affect the objectivity of this work.

Acknowledgements

We would like to thank David Knight at Innospec Ltd. for breaking open the fuel injectors. This research is funded and supported by the Engineering and Physical Sciences Research Council (EPSRC) and Innospec Ltd. The project is part of the Centre for Doctoral Training in Carbon Capture and Storage and Cleaner Fossil Energy (EPSRC grant no. EP/L016362/1). The EPSRC is also gratefully acknowledged for the Strategic Equipment grant '3D OrbiSIMS: Label free chemical imaging of materials, cells and tissues' funding that supported this work (grant no. EP/P029868/1). Rian Griffiths is funded by a University of Nottingham Anne McLaren Fellowship. We would also like to thank Giles Franche for helpful discussions around AP-MALDI analysis of the samples. We thank Intertek USA for providing photographs of the engine testing rig.

References

1 F. Zhao, M. C. Lai and D. L. Harrington, Automotive spark-ignited direct-injection gasoline engines, *Prog. Energy Combust. Sci.*, 1999, **25**(5), 437–562. Available from: **https://www.sciencedirect.com/science/article/pii/S0360128599000040**.

2 H. Xu, C. Wang, X. Ma, A. K. Sarangi, A. Weall and J. Krueger-Venus, Fuel injector deposits in direct-injection spark-ignition engines, *Prog. Energy Combust. Sci.*, 2015, **50**,

63–80. Available from: https://www.sciencedirect.com/science/article/pii/S0360128515000131.
3 C. Wang, H. Xu, J. M. Herreros, J. Wang and R. Cracknell, Impact of fuel and injection system on particle emissions from a GDI engine, *Appl. Energy*, 2014, **132**, 178–191. Available from: https://www.sciencedirect.com/science/article/pii/S0306261914005868.
4 H. Song, J. Xiao, Y. Chen and Z. Huang, The effects of deposits on spray behaviors of a gasoline direct injector, *Fuel*, 2016, **180**, 506–513. Available from: https://www.sciencedirect.com/science/article/pii/S0016236116302320.
5 T. Badawy, M. A. Attar, H. Xu and A. Ghafourian, Assessment of gasoline direct injector fouling effects on fuel injection, engine performance and emissions, *Appl. Energy*, 2018, **220**, 351–374. Available from: https://www.sciencedirect.com/science/article/pii/S0306261918303623.
6 W. Zhang, X. Ma, L. Xinhui and S. Shuai, *Impact of Fuel Properties on GDI Injector Deposit Formation and Particulate Matter Emissions*, SAE Technical Papers, 2020, 01(0388).
7 R. Zhu, J. Hu, X. Bao, L. He and L. Zu, Effects of aromatics, olefins and distillation temperatures (T50 & T90) on particle mass and number emissions from gasoline direct injection (GDI) vehicles, *Energy Policy*, 2017, **101**, 185–193. Available from: https://www.sciencedirect.com/science/article/pii/S0301421516306188.
8 J. Barker, S. Cook and P. Richards, *Sodium Contamination of Diesel Fuel, its Interaction with Fuel Additives and the Resultant Effects on Filter Plugging and Injector Fouling*, 2013. DOI: 10.4271/2013-01-2687.
9 L. S. G. Teixeira, J. C. Souza, H. C. dos Santos, L. A. M. Pontes, P. R. B. Guimarães, E. v. Sobrinho, *et al.*, The influence of Cu, Fe, Ni, Pb and Zn on gum formation in the Brazilian automotive gasoline, *Fuel Process. Technol.*, 2007, **88**(1), 73–76. Available from: https://www.sciencedirect.com/science/article/pii/S0378382006001275.
10 F. Pradelle, S. L. Braga, A. R. F. A. Martins, F. Turkovics and R. N. C. Pradelle, Gum Formation in Gasoline and Its Blends: A Review, *Energy Fuels*, 2015, **29**(12), 7753–7770, DOI: 10.1021/acs.energyfuels.5b01894.
11 M. K. Edney, J. Barker, J. Reid, D. J. Scurr and C. E. Snape, Recent Advances in the Analysis of GDI and Diesel Fuel Injector Deposits, *Fuel*, 2020, **272**, 117682. Available from: https://www.sciencedirect.com/science/article/pii/S0016236120306773?dgcid=author.
12 R. I. Slavchov, S. Mosbach, M. Kraft, R. Pearson and S. v. Filip, An adsorption-precipitation model for the formation of injector external deposits in internal combustion engines, *Appl. Energy*, 2018, **228**, 1423–1438. Available from: https://www.sciencedirect.com/science/article/pii/S0306261918309991.
13 R. I. Slavchov, M. Salamanca, D. Russo, I. Salama, S. Mosbach, S. M. Clarke, *et al.*, The role of NO2 and NO in the mechanism of hydrocarbon degradation leading to carbonaceous deposits in engines, *Fuel*, 2020, **267**, 117218. Available from: https://www.sciencedirect.com/science/article/pii/S0016236120302131.
14 F. Pickl, M. Russer, M. Hauenstein and M. Wensing, Modelling and understanding deposit formation and reduction in combustion engines – Application to the concrete case of internal GDI injector deposit, *Fuel*, 2019, **236**, 284–296. Available from: https://www.sciencedirect.com/science/article/pii/S0016236118315114.
15 N. Wang, Y. Zhi, Y. Wei, W. Zhang, Z. Liu, J. Huang, *et al.*, Molecular elucidating of an unusual growth mechanism for polycyclic aromatic hydrocarbons in confined space, *Nat. Commun.*, 2020, **11**(1), 1079, DOI: 10.1038/s41467-020-14493-9.
16 W. Zhang, J. T. Andersson, H. J. Räder and K. Müllen, Molecular characterization of large polycyclic aromatic hydrocarbons in solid petroleum pitch and coal tar pitch by high resolution MALDI ToF MS and insights from ion mobility separation, *Carbon*, 2015, **95**, 672–680. Available from: https://www.sciencedirect.com/science/article/abs/pii/S0008622315301731.
17 J. Barker, J. Reid, M. Piggott, M. W. Fay, A. Davies and C. Parmenter, *et al.*, *The Characterisation of Diesel Internal Injector Deposits by Focused Ion-Beam Scanning Electron Microscopy (FIB-SEM), Transmission Electron Microscopy (TEM), Atomic Force Microscopy and Raman Spectroscopy*, in *JSAE/SAE 2015 International Powertrains, Fuels & Lubricants Meeting*, SAE International, 2015. DOI: 10.4271/2015-01-1826.
18 R. Venkataraman and S. Eser, Characterization of deposits formed on diesel injectors in field test and from thermal oxidative degradation of n-hexadecane in a laboratory reactor, *Chem. Cent. J.*, 2008, **2**, 25. Available from: https://www.ncbi.nlm.nih.gov/pubmed/19091086.
19 R. Taylor, G. J. Langley, H. W. Kroto and D. R. M. Walton, Formation of C60 by pyrolysis of naphthalene, *Nature*, 1993, **366**(6457), 728–731, DOI: 10.1038/366728a0.
20 R. K. E. Gover, T. W. Chamberlain, P. J. Sarre and A. N. Khlobystov, Piecing Together Large Polycyclic Aromatic Hydrocarbons and Fullerenes: A Combined ChemTEM Imaging and MALDI-ToF Mass Spectrometry Approach, *Front. Chem.*, 2021, **9**, Available from: https://www.frontiersin.org/article/10.3389/fchem.2021.700562.
21 E. Reizer, B. Viskolcz and B. Fiser, Formation and growth mechanisms of polycyclic aromatic hydrocarbons: A mini-review, *Chemosphere*, 2022, **291**, 132793. Available from: https://www.sciencedirect.com/science/article/pii/S0045653521032653.
22 M. K. Passarelli, A. Pirkl, R. Moellers, D. Grinfeld, F. Kollmer, R. Havelund, *et al.*, The 3D OrbiSIMS—label-free metabolic imaging with subcellular lateral resolution and high mass-resolving power, *Nat. Methods*, 2017, **14**, 1175, DOI: 10.1038/nmeth.4504.
23 M. Edney, J. Lamb, M. Spanu, E. Smith, E. Steer, E. Wilmot, *et al.*, Spatially Resolved Molecular Compositions of Insoluble Multilayer Deposits Responsible for Increased Pollution from Internal Combustion Engines, *ACS Appl. Mater. Interfaces*, 2020, **12**(45), 51026–51035.

24 M. K. Edney, A. M. Kotowska, M. Spanu, G. F. Trindade, E. Wilmot, J. Reid, *et al.*, Molecular Formula Prediction for Chemical Filtering of 3D OrbiSIMS Datasets, *Anal. Chem.*, 2022, **94**(11), 4703–4711, DOI: **10.1021/acs.analchem.1c04898**.

25 A. Tran, A. Monreal, E. Moskovets, H. C. Aguilar and J. W. Jones, Rapid Detection of Viral Envelope Lipids Using Lithium Adducts and AP-MALDI High-Resolution Mass Spectrometry, *J. Am. Soc. Mass Spectrom.*, 2021, **32**(9), 2322–2333.

26 L. Matjacic, M. P. Seah, G. F. Trindade, A. Pirkl, R. Havelund, J. L. Vorng, *et al.*, OrbiSIMS metrology Part I: Optimisation of the target potential and collision cell pressure, *Surf. Interface Anal.*, 2022, **54**(4), 331–340, DOI: **10.1002/sia.7058**.

27 *National Research Council (US) Committee on Pyrene and Selected Analogues. Polycyclic Aromatic Hydrocarbons: Evaluation of Sources and Effects*, Washington (DC), National Academies Press (US), 1983, Appendix A, Lists of Polycyclic Aromatic Hydrocarb. Available from: **https://www.ncbi.nlm.nih.gov/books/NBK217760/**.

28 E. Cha, E. S. Jeong, S. B. Han, S. Cha, J. Son, S. Kim, *et al.*, Ionization of Gas-Phase Polycyclic Aromatic Hydrocarbons in Electrospray Ionization Coupled with Gas Chromatography, *Anal. Chem.*, 2018, **90**(6), 4203–4211, DOI: **10.1021/acs.analchem.8b00401**.

29 G. W. Lien, C. Y. Chen and C. F. Wu, Analysis of polycyclic aromatic hydrocarbons by liquid chromatography/tandem mass spectrometry using atmospheric pressure chemical ionization or electrospray ionization with tropylium post-column derivatization, *Rapid Commun. Mass Spectrom.*, 2007, **21**(22), 3694–3700, DOI: **10.1002/rcm.3267**.

30 K. Kashiwa, M. Arai and Y. Kobayashi, *Study on PAHs and PM Formed by Benzene Pyrolysis. Vol. 2, SAE International Journal of Advances and Current Practices in Mobility*, SAE International, 2019, pp. 426–433.

31 M. D. Boot, M. Tian, E. J. M. Hensen and S. Mani Sarathy, Impact of fuel molecular structure on auto-ignition behavior – Design rules for future high performance gasolines, *Prog. Energy Combust. Sci.*, 2017, **60**, 1–25, DOI: **10.1016/j.pecs.2016.12.001**.

32 D. S. N. Parker, R. I. Kaiser, T. P. Troy and M. Ahmed, Hydrogen Abstraction/Acetylene Addition Revealed, *Angew. Chem., Int. Ed.*, 2014, **53**(30), 7740–7744, DOI: **10.1002/anie.201404537**.

33 B. Shukla and M. Koshi, A novel route for PAH growth in HACA based mechanisms, *Combust. Flame*, 2012, **159**(12), 3589–3596. Available from: **https://www.sciencedirect.com/science/article/pii/S0010218012002465**.

34 C. McRae, C. E. Snape, C. G. Sun, D. Fabbri, D. Tartari, C. Trombini, *et al.*, Use of Compound-Specific Stable Isotope Analysis to Source Anthropogenic Natural Gas-Derived Polycyclic Aromatic Hydrocarbons in a Lagoon Sediment, *Environ. Sci. Technol.*, 2000, **34**(22), 4684–4686, DOI: **10.1021/es0010002**.

35 L. Liu, S. Chen, H. Xu, Q. Zhu and H. Ren, Effect of alkyl substituent for cyclohexane on pyrolysis towards sooting tendency from theoretical principle, *J. Anal. Appl. Pyrolysis*, 2022, **161**, 105386. Available from: **https://www.sciencedirect.com/science/article/pii/S0165237021003727**.

36 R. C. Anderson, Acetylene as an Intermediate in Combustion of Petroleum Hydrocarbons, in *Literature of the Combustion of Petroleum*, American Chemical Society, 1958, pp. 49–57. (Advances in Chemistry; vol. 20). DOI: **10.1021/ba-1958-0020.ch005**.

37 B. Shukla and M. Koshi, A highly efficient growth mechanism of polycyclic aromatic hydrocarbons, *Phys. Chem. Chem. Phys.*, 2010, **12**(10), 2427–2437, DOI: **10.1039/B919644G**.

38 T. Miyayama, N. Sanada, S. R. Bryan, J. S. Hammond and M. Suzuki, Removal of Ar+ beam-induced damaged layers from polyimide surfaces with argon gas cluster ion beams, *Surf. Interface Anal.*, 2010, **42**(9), 1453–1457, DOI: **10.1002/sia.3675**.

39 D. F. Yancey and C. Reinhardt, Damage and repair of organic and inorganic surfaces by Ar+ ion and gas cluster ion beam sputtering, *J. Electron Spectrosc. Relat. Phenom.*, 2019, **231**, 104–108. Available from: **https://www.sciencedirect.com/science/article/pii/S0368204817301858**.

40 L. R. Snyder and B. E. Buell, Nitrogen and oxygen compound types in petroleum. A general separation scheme, *Anal. Chem.*, 1968, **40**(8), 1295–1302, DOI: **10.1021/ac60264a004**.

41 L. R. Snyder, Petroleum nitrogen compounds and oxygen compounds, *Acc. Chem. Res.*, 2002, **3**(9), 290–299.

42 G. H. C. Prado, Y. Rao and A. de Klerk, Nitrogen Removal from Oil: A Review, *Energy Fuels*, 2016, **31**(1), 14–36.

43 J. G. Speight, *The Chemistry and Technology of Petroleum*, Taylor & Francis, 5th edn, 2014. (Chemical Industries). Available from: **https://books.google.co.uk/books?id=Pp_AAgAAQBAJ**.

44 T. Rodríguez-Cabo, M. Moniruzzaman, I. Rodríguez, M. Ramil, R. Cela and S. H. Gan, Time-of-flight accurate mass spectrometry identification of quinoline alkaloids in honey, *Anal. Bioanal. Chem.*, 2015, **407**(20), 6159–6170, DOI: **10.1007/s00216-015-8791-2**.

45 A. Hallberg and A. R. Martin, Mass spectral fragmentation patterns of heterocycles. VI. Carbazole and 1,8-dideuteriocarbazole, *J. Heterocycl. Chem.*, 1984, **21**(3), 837–840, DOI: **10.1002/jhet.5570210339**.

46 D. S. N. Parker, K. RalfI, O. Kostko, T. P. Troy, M. Ahmed, A. M. Mebel, *et al.*, Gas phase synthesis of (iso)quinoline and its role in the formation of nucleobases in the INTAB - Nitrogen-substituted polycyclic aromatic hydrocarbons (NPAHs) have been proposed to play a key role in the astrochemical evolution of the interstellar mediu, *Astrophys. J.*, 2015, **803**(2), 53. Available from: **https://doi.org/10.1088/0004-637X/803/2/53**.

47 A. Ricca, C. W. Bauschlicher and E. L. O. Bakes, A Computational Study of the Mechanisms for the Incorporation of a Nitrogen Atom into Polycyclic Aromatic

Hydrocarbons in the Titan Haze, *Icarus*, 2001, **154**(2), 516–521. Available from: **https://www.sciencedirect.com/science/article/pii/S0019103501966941**.

48 T. Yao, B. J. Zhong and K. H. Luo, Compact Chemical Mechanism for Autoignition and Combustion of Methylcyclohexane under Engine Relevant Conditions, *Energy Fuels*, 2017, **31**(10), 11337–11347, DOI: **10.1021/acs.energyfuels.7b01224**.

49 A. Ratkiewicz, Kinetics of the C–C bond beta scission reactions in alkyl radicals, *Phys. Chem. Chem. Phys.*, 2011, **13**(33), 15037–15046, DOI: **10.1039/C1CP21229J**.